Angewandte Chemie

GDCh

Eine Zeitschrift der Gesellschaft Deutscher Chemiker

www.angewandte.de

WILEY-VCH

RESEARCH ARTICLE

WILEY-VCH

Efficient Electrochemical Nitrate Reduction to Ammonia with Copper Supported Rhodium Cluster and Single-Atom Catalysts

Huimin Liu,[a] Xiuyao Lang,[a] Chao Zhu,[b] Janis Timoshenko,[c] Martina Rüscher,[c] Lichen Bai,[c] Néstor Guijarro,[d] Haibo Yin,[e] Yue Peng,[e] Junhua Li,[e] Zheng Liu,[b] Weichao Wang,[a] Beatriz Roldan Cuenya,[c] and Jingshan Luo*[a]

[a]   H. Liu, X. Lang, Prof. W. Wang, Prof. J. Luo
     Institute of Photoelectronic Thin Film Devices and Technology, Solar Energy Research Center, Key Laboratory of Photoelectronic Thin Film Devices and Technology of Tianjin, Ministry of Education Engineering Research Center of Thin Film Photoelectronic Technology, Renewable Energy Conversion and Storage Center, Nankai University
     Tianjin, China
     E-mail: jingshan.luo@nankai.edu.cn
[b]   Prof. C. Zhu, Prof. Z. Liu
     School of Materials Science and Engineering, Nanyang Technological University Singapore
     Singapore
[c]   J. Timoshenko, M. Rüscher, L. Bai, Prof. B. Cuenya
     Department of Interface Science, Fritz-Haber-Institut der Max-Planck-Gesellschaft
     Berlin, Germany
[d]   Prof. N. Guijarro
     Institute of Electrochemistry, University of Alicante
     Alicante, Spain
[e]   H. Yin, Prof. Y. Peng, Prof. J. Li
     State Key Joint Laboratory of Environment Simulation and Pollution Control, School of Environment, Tsinghua University
     Beijing, China

     Supporting information for this article is given via a link at the end of the document.

Abstract: The electrochemical nitrate reduction reaction (NITRR) provides a promising solution for restoring the imbalance in the global nitrogen cycle while enabling a sustainable and decentralized route to source ammonia. Here, we demonstrate a novel electrocatalyst for NITRR consisting of Rh clusters and single-atoms dispersed onto Cu nanowires (NWs), which delivers a partial current density of 162 mA cm^{-2} for NH$_3$ production and a Faradaic efficiency (FE) of 93% at −0.2 V vs. RHE. The highest ammonia yield rate reached a record value of 1.27 mmol h^{-1} cm^{-2}. Detailed investigations by electron spin resonance, in-situ infrared spectroscopy, differential electrochemical mass spectrometry and density functional theory modeling suggest that the high activity originates from the synergistic catalytic cooperation between Rh and Cu sites, whereby adsorbed hydrogen on Rh sites transfer to vicinal *NO intermediate species adsorbed on Cu promoting the hydrogenation and ammonia formation.

Introduction

Ammonia is the essential chemical and the cornerstone of the large and ever-growing fertilizer industry. It is also a potential hydrogen carrier and can be cracked into H$_2$ and N$_2$ at the destination affording hydrogen on demand. Unlike liquid hydrogen that needs harsh condition to be stored, ammonia can be readily liquefied by increasing pressure to ~10 bar at room temperature, or by cooling to −33℃ at atmospheric pressure.[1] Indeed, ammonia is foreseen to gain momentum as a carbon-free fuel for ships, heavy transport vehicles once direct ammonia fuel cells reach a higher level of maturity.[2]

Currently, the worldwide production of ammonia relies on the Haber-Bosch (HB) process, which consumes about 5.5 EJ of energy every year (~38 GJ/t$_{NH3}$) and emits over 450 million metric tons of carbon dioxide (~2.9 t$_{CO2}$/t$_{NH3}$).[3] With the growing interests of using ammonia in non-agriculture sectors (e.g. energy), the production scale of ammonia and ammonia-related emissions will be further expanded. Thus, to meet the COP21 two-degree scenario (2DS) target[3] for ammonia, there is a compelling need to replace the conventional HB process by alternative sustainable strategies compatible with renewables that could meet the increasing demand. Electrochemical nitrate reduction (NITRR) has the potential of decentralized production of "green" ammonia with an economically-competitive rate.[4] On the one hand, excessive use of fertilizer and other human activities have contributed a lot of nitrate in ground and surface water. Recycling redundant nitrates and converting them to ammonia could add direct economic value to the remediation process.[1, 5] On the other hand, with the development of electrochemical conversion of nitrogen to nitrate via non-thermal plasma techniques and nitrogen oxidation,[6] ammonia production from nitrate is no longer a reversal of the Ostwald process and the production scale can be further extended. Therefore, the NITRR could provide a sustainable alternative to the HB process and simultaneously provide a solution for restoring the imbalance in the global nitrogen cycle.[7]

In the early years, Cu-based catalysts have been reported for the NITRR. However, as the research foothold is only the remediation of nitrate in the environment, most catalysts are designed to produce nitrogen.[8] Although there were a few Cu-based catalysts reported for ammonia synthesis, the in-depth mechanistic studies were lacked. Recently, Cu-based catalysts for NITRR has demonstrated an upsurge in research again,[9] displaying Faradaic efficiencies (FE) greater than 90% and partial current densities for ammonia production close to 100 mA cm^{-2}. However, they usually operated only at very negative applied potentials (around −0.4 ~ −0.7 V vs. RHE), which is

energetically inefficient. It has been argued that the weak adsorption of H on Cu may be the main limiting factor for the NITRR, i.e., only at very negative applied potentials the *H coverage is high enough to maintain a significant surface hydrogenation rate.[10] Therefore, it is expected that by activating the hydrogenation ability of Cu-based catalyst at more positive applied potentials the overpotential for the NITRR could be drastically reduced. Rhodium (Rh) is known to exhibit excellent hydrogen adsorption-desorption features,[11] as demonstrated by its uppermost and centered position in the HER volcano plot. We therefore hypothesize that proper distribution of Rh over Cu sites could patch the poor hydrogenation capabilities of bare Cu and improve the NITRR performance.

Inspired by recent advances in cluster and single-atom catalysis,[12] here we constructed a series of electrodes based on Rh cluster and single-atom supported on Cu NWs (Rh@Cu, henceforth). The NITRR was explored as a function of the Rh-content, revealing a record partial current density for NH_3 production of 162 mA cm^{-2} and a 93% FE at −0.2 V vs. RHE for very low Rh loading (Rh@Cu-0.6%). Importantly, ^{15}N labelling together with NMR experiments confirmed nitrate as the only N-source of the produced ammonia. Mechanistic insights on the reaction gathered by electron paramagnetic resonance (EPR) spectroscopy, in-situ infrared spectroscopy, in-situ Raman spectroscopy, on-line differential electrochemical mass spectrometry (DEMS) and density functional theory (DFT) modeling provided compelling evidences of the synergistic catalytic cooperation between Cu and Rh. The Cu site preferentially stabilizes nitrogen intermediate species, whereas the vicinal Rh supplies the activated H species required for the surface hydrogenation to proceed. Ultimately, ammonia was released as the product.

Results and Discussion

Catalyst preparation and characterization. The electrodes made of Cu_2O NWs were first fabricated as reported in previous work.[13] Then, the Cu_2O NWs were reduced to Cu NWs by electrochemical reduction. Finally, Cu NWs coated with either homogeneously distributed Rh cluster and single-atom (Rh@Cu) or Rh nanoparticles (NP Rh@Cu) were synthesized by galvanic replacement reaction between Cu and Rh^{3+}, as detailed in the Supporting Information. The scanning electron microscopy (SEM) images confirmed the micrometer-long Cu NWs, and the X-ray diffraction (XRD) pattern solely detected the characteristic reflections of Cu without oxide phases (Figure S1). Three different Rh@Cu catalysts in terms of different Rh loading were prepared, namely samples with 12.5% (NP Rh@Cu-12.5%), 0.6% (Rh@Cu-0.6%) and 0.3% (Rh@Cu-0.3%) of Rh, respectively. The SEM and transmission electron microscopy (TEM) images of Rh@Cu-0.6% (Figure 1a-b and S2-S3), NP Rh@Cu-12.5% (Figure S4, S6) and Rh@Cu-0.3% (Figure S7) samples recorded before and after the NITRR did not reveal major structural variations on the NWs. This can be attributed to the small feature size of the Rh deposited on the surface in all cases and the stability under cathodic operation of the Cu NWs. Indeed, XRD patterns for all samples did not reveal any change upon the NITRR tests, which confirmed the robustness of the Cu electrodes and the low Rh contents (Figure S8 and 1i). In order

to better assess the presence of Rh, elemental mapping was performed. Overall, the content of Rh estimated by energy-dispersive X-ray spectroscopy (EDS) and inductive coupled plasma-optical emission spectroscopy (ICP-OES) matched well, that is, 12.5% (Figure S4-6), 0.6% (Figure 1c-g) and 0.3% (Figure S7), respectively, and barely changed upon operation. In addition, the aberration-corrected high-angle annular dark-field scanning transmission electron microscopy (AC-HAADF-STEM) was employed to further detect Rh atoms based on contrast difference. As shown in Figure 1h, many bright dots and atom-sized features attributed to individual Rh atoms as well as very small Rh clusters can be discerned on the surface of Cu (111) in Rh@Cu-0.6%. In contrast, the higher loading of Rh@Cu-12.5% leads to Rh nanoparticles with a characteristic lattice fringe of 0.220 nm corresponding to Rh (111), which can be well differentiated from the characteristic lattice spacing of 0.209 nm assigned to Cu (111) (Figure S4). Finally, for the Rh@Cu-0.3% sample, since the amount of Rh is even lower, we speculated that Rh in this sample is also in the form of single atoms and clusters.

We also used X-ray absorption spectroscopy (XAS), including X-ray absorption near edge structure (XANES) and extended X-ray absorption fine structure (EXAFS) to analyze the chemical state and local structure of Rh in Rh@Cu-0.6%. The Rh K-edge XANES spectrum for Rh@Cu-0.6% lies in between those corresponding to Rh foil and Rh_2O_3 reference samples. Indeed, linear combination analysis of XANES spectra (see the inset of Figure 1j), where the spectrum for Rh@Cu-0.6% sample is fitted with a linear combination of spectra for Rh foil and Rh_2O_3, provides a good agreement with experimental Rh@Cu-0.6% sample spectrum, and suggests that ca. 63% of Rh is in reduced form and ca. 37% of Rh is oxidized. The presence of oxidized Rh species can be attributed to the sample being placed in air so that its surface is inevitably oxidized. During the subsequent NITRR test, the applied potentials is from 0 V to −0.5 V vs. RHE, which is much lower than the standard reduction potential of Rh^{3+}/Rh (0.758 V vs. RHE),[14] thus we expect that the oxide cannot be retained and the main form of Rh in the working catalyst is Rh^0 during NITRR test. The frequency of Rh K-edge EXAFS spectra at large k-values matches well with that of EXAFS spectrum for Rh foil (Figure 1k). This suggests that the distances between Rh and neighboring metal atoms are very closed to these distances in Rh foil, and strongly supports the formation of Rh-rich phase. Note that in the case of homogeneous Rh alloying with Cu, we would expect a significant contraction of interatomic distances (and, hence, a decrease in EXAFS frequencies) due to a very large Cu to Rh ratio in our sample, and the significantly smaller lattice constant of metallic copper compare to metallic rhodium. Combined with AC-HAADF-STEM, these XAS results show that part of Rh exists in the form of small clusters in Rh@Cu-0.6%. Fourier-transformed (FT) EXAFS spectra (Figure 1l) confirm conclusions from the visual examination of XANES and EXAFS data. FT-EXAFS spectra are dominated by three peaks. The first one at ca. 1.7 Å (phase uncorrected) was assigned to Rh-O bond, and the peaks between ca. 2.1 Å and 2.5 Å were assigned to a superposition of Rh-Cu and Rh-Rh bond contributions. This provides compelling evidence of the existence of single atom Rh and Rh clusters.

2
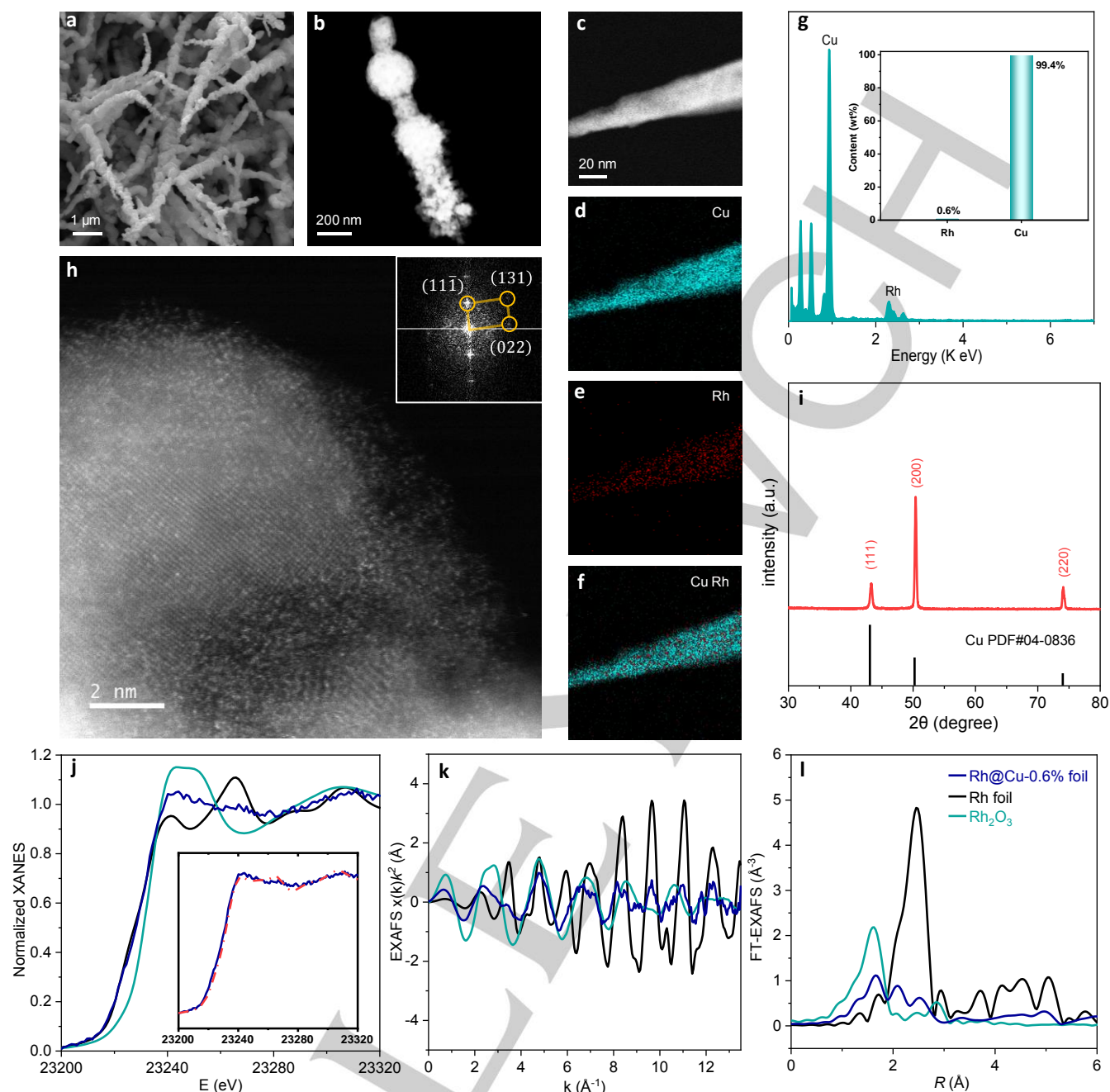
Figure 1. Structure and composition characterization of the Rh@Cu-0.6% sample. (a) Scanning electron microscopy (SEM) image, (b) High-angle annular dark-field scanning transmission electron microscopy (HAADF-STEM), (c-f) HAADF-STEM image and elemental mapping images, (g) energy-dispersive X-ray spectroscopy (EDS) and the insert map is the content of Rh and Cu obtained by inductively coupled plasma-optical emission spectroscopy (ICP-OES), (h) aberration-corrected high-angle annular dark-field scanning transmission electron microscopy (AC-HAADF-STEM) image and (i) X-ray diffraction (XRD) pattern of Rh@Cu-0.6% after NITRR test under −0.2 V vs. RHE. (j) Rh K-edge X-ray absorption near edge structure (XANES), (k) extended X-ray absorption fine structure (EXAFS) and (l) Fourier-transformed EXAFS spectra for Rh@Cu-0.6% foil. Spectra for Rh foil and Rh_2O_3 are also shown for comparison. Inset in (j) shows the linear combination fit (red dashed line) for Rh K-edge XANES spectrum, using the spectra of Rh foil and Rh_2O_3 as references.

EXAFS data fitting was next performed for quantitative analysis. The results of the fitting are summarized in Figure S9 and Table S1. Good agreement between experimental and modeled data (Figure S9), and the reasonable values of R-factors (Table S1) support the validity of the fitting models. The obtained values for Rh-O and Rh-Rh bond lengths and disorder factors are in reasonable agreement with those in bulk reference materials. The Rh-Cu bond length obtained for Rh@Cu-0.6% is between the Rh-Rh bond length (2.64±0.04 Å) and the typical

bond lengths in metallic Cu (ca. 2.56 Å), as expected for bimetallic systems.[15] Slightly lower Rh-Rh bond length observed for Rh@Cu-0.6% sample (2.64±0.04 Å) than that in Rh foil (2.68 Å) may, in turn, suggest that the size of Rh clusters is small, resulting in relatively large contribution of compressed Rh-Rh distances at the cluster surface[16] (although the contraction of distances due to partial alloying with Cu cannot be excluded).

We noted that the obtained coordination numbers for Rh@Cu-0.6% are lower than the corresponding values of bulk

3

materials due to sample-averaging effect: for a mixture of phases, the coordination numbers yielded by EXAFS fitting correspond to N^{true}/x, where x is the concentration of the particular Rh species, and N^{true} is the actual average number of nearest neighbors of given type in this species. By comparing the Rh-O coordination number, obtained from EXAFS fitting (2.6±0.3), with the Rh-O coordination number in bulk oxide (6), we conclude that ca. x_{oxide} = 43% of the Rh is oxidized while ca. x_{metal}=57% of Rh thus is in metallic state, which is in a good agreement with the results from XANES analysis. By correcting the Rh-Rh and Rh-Cu coordination numbers from EXAFS fit using this x_{metal} value, we obtained the true number of Rh and Cu neighbors for each Rh atom in metallic phases, namely N_{Rh-Rh}^{true} = 4.7±0.7 and N_{Rh-Cu}^{true} = 4+1. Further we assumed the simplest case, where only two different metallic Rh species are present – pure Rh clusters and Rh single atoms incorporated in pure Cu. Following a similar argument, from the comparison of N_{Rh-Cu}^{true} with the expected coordination number for Rh embedded in fcc-type copper (12), we conclude that ca. 33% of the metallic rhodium forms single atom Rh species within copper

matrix. The remaining 66% of metallic Rh is thus present in form of metallic Rh clusters.

Activity and selectivity for NITRR to ammonia. To explore the NITRR performance of the Rh@Cu electrocatalysts, we first recorded linear sweep voltammograms using 0.1 M Na_2SO_4 as supporting electrolytes (pH was adjusted to 11.5) both with and without 0.1 M KNO_3 as nitrogen source. As depicted in Figure 2a, the current density of Rh@Cu catalysts with various Rh content drastically increases in the presence of nitrate. The Rh@Cu-0.6% sample shows the maximum current density and a sharp onset at 0.2 V vs. RHE. As the potential becomes negative, HER and NITRR compete. However, the number of electrons transferred for HER is less than that required for NITRR, and the current appears flat. When the potential becomes more negative, HER competition dominates. At high (more negative) applied potentials, especially when looking at curves of Rh@Cu-0.6% and Rh@Cu-12.5%, the current decreases in a rather irregular fashion. This has been ascribed to the significant hydrogen production occurring at the electrodes' surface, where the generated hydrogen bubbles disturb the electrolyte near the electrode.
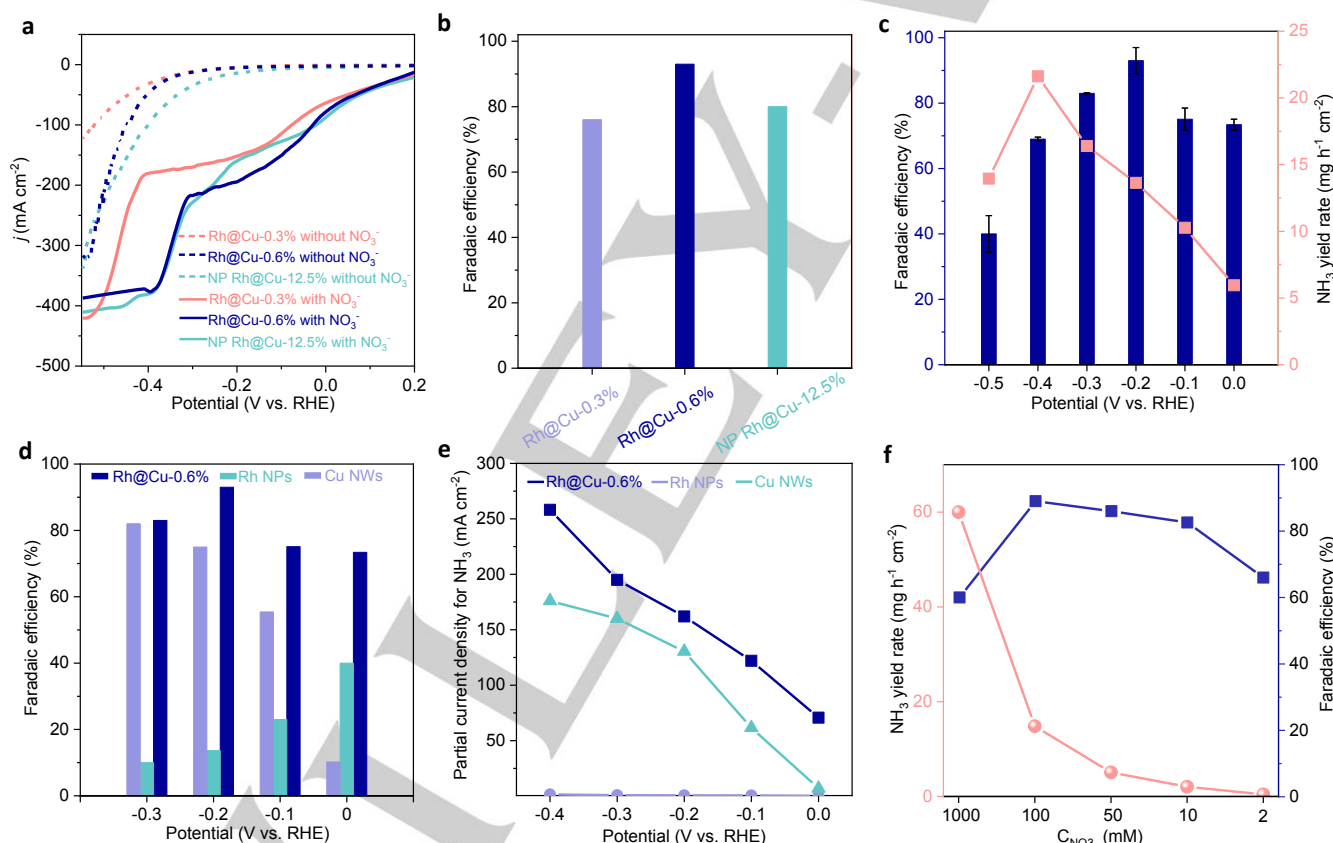

Figure 2. Electrocatalytic performance of Rh@Cu systems. (a) Linear sweep voltammograms of Rh@Cu-0.3%, Rh@Cu-0.6% and NP Rh@Cu-12.5% in 0.1 M Na_2SO_4 electrolyte (pH 11.5) in the absence of NO_3^- (dotted line) and in the presence of NO_3^- (solid line). (b) FE of NITRR to ammonia over Rh@Cu-0.3%, Rh@Cu-0.6% and NP Rh@Cu-12.5% at −0.2 V vs. RHE. (c) Potential-dependent yield rate and FE of ammonia over Rh@Cu-0.6%. (d) Potential-dependent FE of ammonia over Cu NWs, Rh@Cu-0.6% and carbon cloth loaded with Rh NPs. (e) NITRR partial current densities for NH_3 of Cu NWs, Rh@Cu-0.6% and carbon cloth loaded with Rh NPs under applied potentials of 0, −0.1, −0.2, −0.3 and −0.4 V vs. RHE. (f) Yield rate and FE of NITRR to ammonia on Rh@Cu-0.6% in 0.1 M Na_2SO_4 electrolyte (pH 11.5) with 2 mM, 10 mM, 50 mM, 100 mM and 1000 mM NO_3^-.

Furthermore, the product analysis by the colorimetric method (Figure S10-11) confirmed that the Rh@Cu-0.6% sample displayed the highest performance. Both lower (Rh@Cu-0.3%) and higher (NP Rh@Cu-12.5%) Rh loadings led to a lower performance (Figure 2b and Figure S12-13). The sample with too little Rh doping may not have obvious synergistic effect

between Cu and Rh, while too much Rh loading will lead to the enhancement of competing HER. Therefore, Rh@Cu-0.6% was the focus of our investigation. Further characterization of the reaction products demonstrated a steady increase of ammonia production up to −0.4 V vs. RHE, reaching a record value of 21.61 mg $h^{-1}cm^{-2}$, or 1.27 mmol $h^{-1}cm^{-2}$ (see Table S2 or Figure

4

S14), whereas FE values hit a maximum of 93% at −0.2 V vs. RHE (Figure 2c). The slight deterioration of these values at more negative potentials could be ascribed to the competing HER. The FE of Rh@Cu-0.6% is obviously improved compared with bare Cu foil, Cu NWs and Rh nanoparticles (NPs) (Figure 2d and S15-18). The partial current density for ammonia production of Rh@Cu-0.6% reached 162.0 mA cm^{-2} at −0.2 V vs. RHE (Figure 2e and Table S2), which was also much higher than Rh NPs and had a 24.6% increase compared to Cu NWs (130.0 mA cm^{-2}). In addition, the potential at which the NH_3 production reaches peak FE for the Rh@Cu-0.6% sample is 200 mV more positive than that of pure Cu NWs (Figure 2d, S16). Overall, the above results provide compelling evidence of the synergy between Rh and Cu NWs when appropriately interfaced. Finally, the influence of the nitrate concentration on the performance

was assessed and the optimized FE for ammonia production was achieved in electrolyte with 100 mM NO_3^- (Figure 2f). The FE for ammonia production was slightly reduced as the NO_3^- concentration decreased, likely because of the increased contribution of the competing HER. Interestingly, the FE of ammonia production decreased with the increase of NO_3^- concentration to 1 M. We hypothesize that the large concentration of produced ammonia in this case might not be removed rapidly from the catalyst surface in time, resulting in the deactivation of the active sites for NITRR. The maximum FE of Rh@Cu-0.6% for NITRR in 0.1 M Na_2SO_4 with 0.1 M NO_3^- and 0.1 M PBS (pH 7) with 0.1 M NO_3^- is 96% and 80%, respectively. These demonstrate that Rh@Cu-0.6% also displays a good NITRR performance in neutral electrolytes, which is promising for environmental application (Figure S19-20).
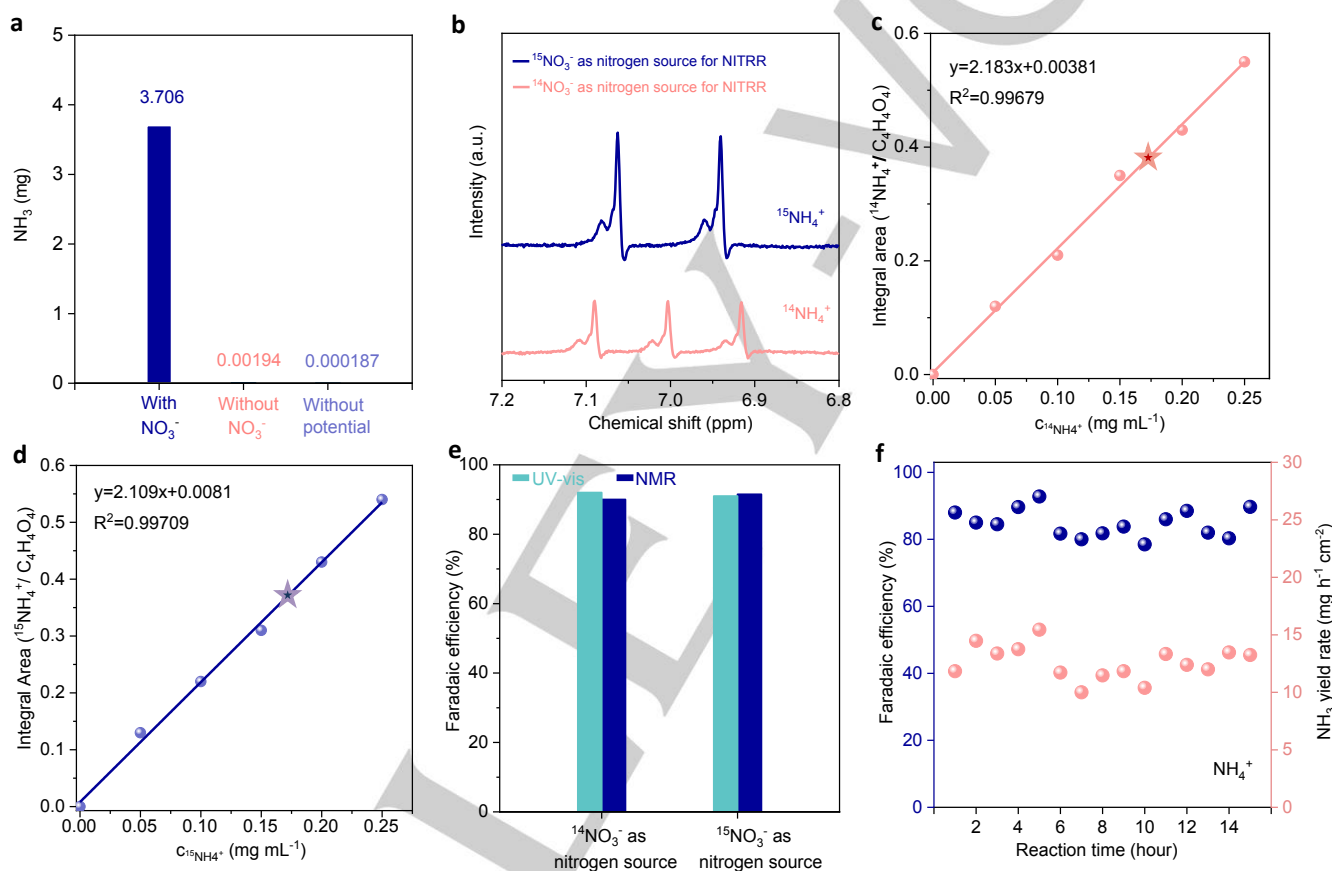
Figure 3. Control tests and isotope labeling experiments of Rh@Cu-0.6%. (a) The ammonia yield of electrocatalysis over Rh@Cu-0.6% in 0.1 M Na_2SO_4 electrolyte (pH 11.5) with NO_3^- at −0.2 V vs. RHE, without NO_3^- at −0.2 V vs. RHE and without applied potential in the presence of NO_3^-, respectively. (b) ^{1}H nuclear magnetic resonance (NMR) spectra of the electrolyte after electrocatalytic NITRR over Rh@Cu-0.6% at −0.2 V vs. RHE using $^{15}NO_3^-$ and $^{14}NO_3^-$ as the nitrogen source. (c) The standard curve of integral area ($^{14}NH_4^+$/ $C_4H_4O_4$) as a function of $^{14}NH_4^+$ concentration. The star represents the concentration of $^{14}NH_4^+$ after NITRR. (d) The standard curve of integral area ($^{15}NH_4^+$/ $C_4H_4O_4$) as a function of $^{15}NH_4^+$ concentration. The star represents the concentration of $^{15}NH_4^+$ after NITRR. (e) FE of NITRR at −0.2 V vs. RHE using $^{15}NO_3^-$ and $^{14}NO_3^-$ as the nitrogen source, detected by colorimetric method and nuclear magnetic methods. (f) Yield rate and FE of ammonia over Rh@Cu-0.6% under the applied potential of −0.2 V vs. RHE during 15 periods of 1 h electrocatalytic NITRR.

To confirm the origin of the nitrogen incorporated in the synthesized ammonia, several control experiments were undertaken.[17] Firstly, the yield of synthesized ammonia was monitored in the presence of NO_3^- and under open circuit conditions, that is, without current flowing through the cell. This experiment showed a negligible amount of ammonia. Likewise, under applied potential, we did not detect obvious ammonia production unless nitrates were added in the solution (Figure 3a). Overall, these results evidence the direct correlation between the presence of NO_3^- in solution and generation of ammonia.

Secondly, to unambiguously verify that ammonia originates from NO_3^-, isotope labelling experiments wherein NITRR were carried out in the presence of $^{14}NO_3^-$ or $^{15}NO_3^-$ followed by product identification and quantifications via ^{1}H NMR. The characteristic splitting of the ^{1}H resonance into three symmetric signals in the case of using $^{14}NO_3^-$ and the corresponding splitting into two signals when using $^{15}NO_3^-$, evidence the formation of $^{14}NH_4^+$ and $^{15}NH_4^+$, respectively (Figure 3b and S21). We confirmed that the concentrations of detected $^{14}NH_4^+$ and $^{15}NH_4^+$ are virtually the same (Figure 3c-d). These data further corroborated that the

5

NO_3^- in solution is the only source of nitrogen during the electrochemical synthesis of ammonia. Moreover, the calculated FEs of ammonia measured by colorimetric method and ^1H NMR spectra method were compared, and the results are consistent (Figure 3e). In addition, the ammonia yield rate, FE and current density of Rh@Cu-0.6% showed no obvious decay after 15 periods of 1 h electrocatalytic NITRR (Figure 3f and Figure S22). Long-term and continuous electrocatalytic NITRR of Rh@Cu-0.6% was also explored by continuously flowing electrolyte to replenish the constantly consumed NO_3^-, and the FE can still maintain 80% after 30 h test, demonstrating excellent stability. The TEM and EDS of Rh@Cu-0.6% after NITRR for 30 h proved the stability of the structure (Figure S23).

Mechanism study and DFT calculation. We next sought to understand the origin of the remarkable performance of the Rh@Cu electrocatalyst for NITRR, especially at low overpotential. For instance, at −0.1 V vs. RHE, it was found that the production of ammonia for the optimized Rh@Cu-0.6% electrode was over 100 times higher than that of Rh NPs, and 2 times higher than that of Cu NWs (Figure S24). It is plausible to consider Cu as the main active site while the Rh site acts as a promoter. The experimental results of less activity of Rh@Cu-15% compared to Rh@Cu-0.6% confirm that the introduction of a small amount of Rh into Cu can promote ammonia production, but excess Rh will promote the HER due to the strong adsorption capacity of Rh to H (Figure S25). Therefore, we speculate that the introduction of Rh promotes the hydrogenation step of NITRR. The kinetic isotope experiments indicated that when H_2O solvent is replaced by D_2O to carry out the NITRR, the FEs of ammonia production on Cu NWs and Rh@Cu-0.6% do not change significantly, but both the current density and ammonia yield rate of Cu NWs are significantly lower. In comparison, the current density and ammonia yield rate of Rh@Cu-0.6% do not change significantly when H_2O is replaced to D_2O (Figure S26). This indicates that the hydrogenation step of Cu NWs for NITRR is the rate-limiting step. After introducing Rh, the hydrogenation step of Rh@Cu-0.6% is no longer rate-limiting. Therefore, this result suggests that the introduction of Rh promotes the hydrogenation step in NITRR. In-situ infrared spectroscopy (IR) results show that only a weak peak corresponding to -NH_2 can be detected from −0.1 V vs. RHE when pure Cu NWs catalyzes NITRR, while an obvious peak corresponding to -NH_2 is noticed from 0.2 V vs. RHE when Rh@Cu-0.6% catalyzes NITRR (Figure 4a). Since Rh displays a near-optimum H adsorption Gibbs free energy, we speculate that the incorporation of Rh drastically improves the surface adsorption of H in the electrode, which could promote the hydrogenation of the intermediate nitrogen species adsorbed on the nearby Cu sites by a hydrogen transfer mechanism at low applied potentials.[18]

In order to test our hypothesis, we monitored the formation of H radical (H•) upon running HER by EPR using dimethyl-1-pyrroline-N-oxide (DMPO) as the radical trapping reagent.[19] The *H-adsorbed on the catalyst surface during HER has two destinies, which can be dimerized to H_2, or desorb from the catalyst surface to the solution and form H• radical trapped by DMPO.[20] Under alkaline conditions, the overall HER performance is limited by the ability to adsorb hydrogen. In view of the trend in the HER performance, i.e, Rh NPs > Rh@Cu-0.6% > Cu NWs, we could anticipate the poor *H-adsorption

characteristic of the Cu NWs (Figure S27), which is in good agreement with DFT results (Figure S28). In the absence of nitrate, EPR spectra revealed 9 signals with an intensity ratio of 1:1:2:1:2:1:2:1:1, which indicates the formation of H-DMPO in all cases (Figure 4b). It is worth noting that the intensity of the signals, which is proportional to the concentration of H-DMPO, follows the same trend observed in the HER performance, and further corroborates the low degree of H adsorption on Cu NWs. In comparison, the strong EPR signal obtained for the Rh@Cu-0.6% sample demonstrates an efficient adsorption-desorption of H. Based on the DFT calculation, the adsorption of H on Rh is easier than that of nitrate, and also easier than H on Cu site. Therefore, H preferentially adsorbs on Rh sites compared to Cu sites of Rh@Cu-0.6% (Figure S28-29).

We next investigated whether the *H-adsorbed on Rh site could participate in the hydrogenation of the NITRR intermediates by recording the EPR spectra of the electrolyte after NITRR at −0.1 V vs. RHE (Figure 4c). Interestingly, the H-DMPO signal did not change in the presence of nitrate for Rh NPs, while it became undetectable for Rh@Cu-0.6% and Cu NWs. This result suggests that the H• generated at the surface of Rh@Cu-0.6% and Cu NWs is rapidly consumed in the hydrogenation of adjacent surface-activated nitrogen-containing intermediates. However, the Rh NPs are barely active towards NITRR, which is likely because of its unfavorable adsorption of nitrate with respect to the competing HER reaction steps. These findings support the hypothesis that the NITRR mechanism involves hydrogen transfer steps. It is worth noting that a similar hydrogen transfer mechanism could also be detected on the preliminary studies carried out using a similar system, i.e., Ru@Cu-3.4% (Figure S30). This delivers the highest ammonia yield of 19.42 mg h^{-1} cm^{-2} (1.14 mmol h^{-1} cm^{-2}) and FE of 93.4% at -0.2 V vs. RHE, which is also higher than those of bare Cu NWs. More generally, this supports the notion that the hydrogen transfer mechanism, evidenced in Rh@Cu systems, could be found in a wide variety of metal-supported on Cu electrocatalysts systems (Figure S30).

In order to construct a comprehensive description of the reaction mechanism, on-line differential electrochemical mass spectrometry (DEMS) was utilized to detect the intermediate species generated during the NITRR. Figure 4d and Figure S31 display the mass-to-charge ratio (m/z) signals recorded as a function of time while performing 4 subsequent voltammetry scan cycles (each cycle involves a scan from 0.78 V to −1.42 V vs. RHE). Note that m/z signals at 46, 30, 33 and 17 were detected and tracked, corresponding to NO_2, NO, NH_2OH and NH_3, respectively. The in-situ Raman spectroscopy was also conducted to characterize the valence states of Rh and Cu in Rh@Cu-0.6% during NITRR test (Figure S32). Raman spectroscopy of initial Rh@Cu-0.6% showed characteristic peak of Cu_2O at 218 cm^{-1}, CuO at 298 cm^{-1} and 622 cm^{-1}, Rh_2O_3 at 527 cm^{-1} without applying potential. These agree well with the XAS results which evidenced that Rh on the catalyst surface was partially oxidized in air. As the applied potential decreases (more negative), all peaks decreased gradually and disappeared from 0 V vs. RHE onwards. Therefore, the oxidation states of Rh clusters, single Rh atoms and Cu were mostly zero during NITRR. Based on the DEMS, in-situ Raman results and with the aid of DFT, we proposed a reaction pathway and calculated the corresponding Gibbs free energy of each intermediate over Cu and Rh@Cu-0.6% (Figure 4e and S33-34). The NITRR could be

broken down into a series of deoxygenation reactions, *NO$_3$ → *NO$_2$ → *NO, followed by hydrogenation steps *NO → *NOH → *NH$_2$OH → *NH$_3$ and finally desorption of ammonia. In order to clearly explore the contributions of Rh clusters and Rh single atoms, we calculated both of them. Interestingly, while the incorporation of Rh clusters and Rh single atoms barely affects the deoxygenation steps, it drastically reduces the thermodynamic barrier for hydrogenation. In fact, for pure Cu NWs, the conversion of *NO on Cu into *NOH is a proton-coupled electron transfer step with protons from electrolyte (*NO + H$_2$O + e$^-$ →*NOH + OH$^-$) due to the very little coverage of *H on Cu surface, which involved a high free energy increment

(0.35 eV). In comparison, the hydrogenation process of *NO on Cu into *NOH can be significantly promoted with an energy release of 0.85 eV, when this step is triggered by *H on Rh clusters via in-situ hydrogen transfer without electron transfer (*NO + *H→*NOH) (Figure 4e). When this step is triggered by Rh single atoms, it also involved a low free energy increment (0.01 eV) (Figure S34). Therefore, Rh clusters in Rh@Cu play a more critical role in the in-situ hydrogen transfer during the NITRR catalysis. Overall, the decreased free energy of the subsequent steps accounts for the improved FE and current density when the Rh is supported on Cu NWs.
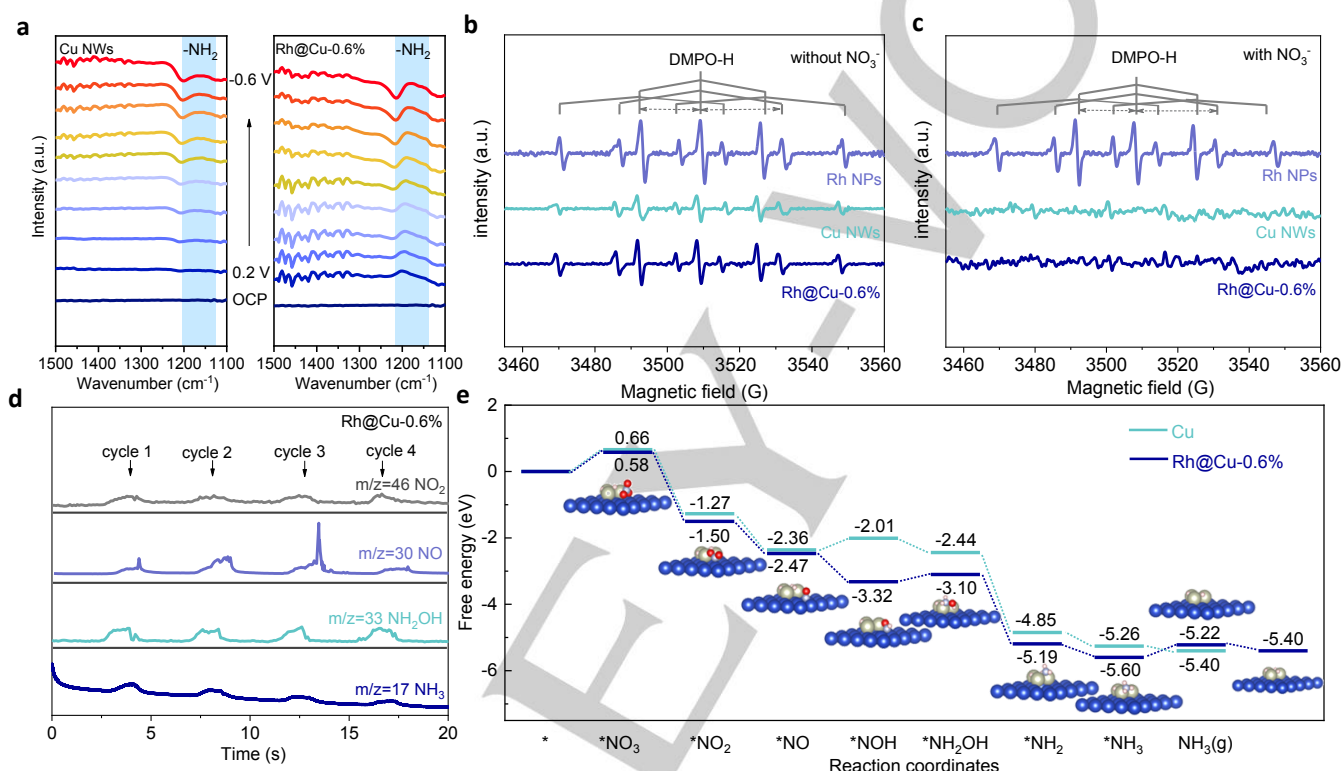
Figure 4. Origin of the NITRR performances over Rh@Cu-0.6%. (a) Electrochemical in-situ infrared spectroscopy (IR) of Rh@Cu-0.6% and Cu NWs with different potentials at 0.1 M Na$_2$SO$_4$ electrolyte (pH 11.5) with 0.1 M KNO$_3$. (b) Electron paramagnetic resonance (EPR) spectra of the solutions obtained after 3 min of electrocatalysis at −0.1 V vs. RHE by Cu NWs, Rh@Cu-0.6% and Rh NPs loading on carbon cloth in 0.1 M Na$_2$SO$_4$ electrolyte (pH 11.5) under argon. (c) EPR spectra of the solutions obtained after 3 min of NITRR at −0.1 V vs. RHE by Cu NWs, Rh@Cu-0.6% and Rh NPs loading on carbon cloth in 0.1 M Na$_2$SO$_4$ electrolyte (pH 11.5) with 0.1 M KNO$_3$ under argon. (d) Differential electrochemical mass spectrometry (DEMS) measurements of NITRR over Rh@Cu-0.6%. (e) Gibbs free energy diagram of various intermediates generated during electrocatalytic NITRR over the pure Cu NWs and Rh@Cu-0.6%, it is assumed that all Rh in Rh@Cu-0.6% exists in the form of clusters. The structural models represent the adsorption form of various intermediates on Rh@Cu-0.6% during NITRR, Cu blue, Rh light gray, N light blue, O red and H light pink atoms.

Conclusion

We have demonstrated that, by interfacing Rh cluster and single-atom Rh with Cu NWs, the hydrogenation steps of ammonia synthesis from NITRR at low applied potentials can be effectively controlled to optimize the catalytic selectivity. Partial current densities up to 162.0 mA cm^{-2} and FE of 93% at potentials as low as −0.2 V vs. RHE were achieved. The highest ammonia yield rate reached 1.27 mmol h^{-1} cm^{-2}, which exceeded that of the state-of-the-art NITRR catalysts. Mechanistic insights sought by utilizing a series of techniques suggested that the excellent activity and efficiency is attributed to the transfer of adsorbed *H from Rh sites to the *NO-adsorbed intermediate species located on Cu sites, thus facilitating the hydrogenation step for ammonia synthesis. This

study not only provides insights for designing NITRR catalysts with high activity and selectivity, but also promotes the further exploration of the NITRR mechanism.

[1]   D. R. MacFarlane, P. V. Cherepanov, J. Choi, B. H. R. Suryanto, R. Y. Hodgetts, J. M. Bakker, F. M. Ferrero Vallana, A. N. Simonov, *Joule* **2020**, *4*, 1186-1205.

[2]   R. F. Service, *Science* **2018**, *361*, 120-123.

[3]   J. Lim, C. A. Fernandez, S. W. Lee, M. C. Hatzell, *ACS Energy Lett.* **2021**, *6*, 3676-3685.

[4]   H. M. Liu, Y. D. Zhang, J. S. Luo, *J. Energy Chem.* **2020**, *49*, 51-58.

[5]   a) C. A. Clark, C. P. Reddy, H. Xu, K. N. Heck, G. Luo, T. P. Senftle, M. S. Wong, *ACS Catal.* **2019**, *10*, 494-509; b) L. Su, D. Han, G. Zhu, H. Xu, W. Luo, L. Wang, W. Jiang, A. Dong, J. Yang, *Nano Lett.* **2019**, *19*, 5423-5430.

[6]   a) C. C. Dai, Y. M. Sun, G. Chen, A. C. Fisher, Z. C. J. Xu, *Angew. Chem. Int. Edit.* **2020**, *59*, 9418-9422; b) L. Q. Li, C. Tang, X. Y. Cui, Y. Zheng, X. S. Wang, H. L. Xu, S. Zhang, T. Shao, K. Davey, S. Z. Qiao, *Angew. Chem. Int. Edit.* **2021**, *60*, 14131-14137.

[7]   I. K. Phebe H. van Langevelde, and M. T. M. Koper, *Joule* **2020**, *5*, 1-5.

[8]   a) S. X. Yang, L. Z. Wang, X. M. Jiao, P. Li, *Int. J. Electrochem. Sci.* **2017**, *12*, 4370-4383; b) Y. M. Zhang, Y. L. Zhao, Z. Chen, L. Q. Wang, P. P. Wu, F. Wang, *Electrochim. Acta* **2018**, *291*, 151e160.

[9]   a) G. F. Chen, Y. Yuan, H. Jiang, S. Y. Ren, L. X. Ding, L. Ma, T. Wu, J. Lu, H. Wang, *Nat. Energy* **2020**, *5*, 605-613; b) Y. Wang, W. Zhou, R. Jia, Y. Yu, B. Zhang, *Angew. Chem. Int. Edit.* **2020**, *59*, 5350-5354; c) Y. H. Wang, A. Xu, Z. Y. Wang, L. S. Huang, J. Li, F. W. Li, J. Wicks, M. C. Luo, D. H. Nam, C. S. Tan, Y. Ding, J. W. Wu, Y. W. Lum, C. T. Din, D. Sinton, G. F. Zheng, E. H. Sargent, *J. Am. Chem. Soc.* **2020**, *142*, 5702-5708.

[10]   J. X. Liu, D. Richards, N. Singh, B. R. Goldsmith, *ACS Catal.* **2019**, *9*, 7052-7064.

[11]   J. K. Nørskov, T. Bligaard, A. Logadottir, J. R. Kitchin, J. G. Chen, S. Pandelov, U. Stimming, *J. Electrochem. Soc.* **2005**, *152*, J23-J26.

[12]   a) H. Yan, H. Cheng, H. Yi, Y. Lin, T. Yao, C. Wang, J. Li, S. Wei, J. Lu, *J. Am. Chem. Soc.* **2015**, *137*, 10484-10487; b) B. Qiao, A. Wang, X. Yang, L. F. Allard, Z. Jiang, Y. Cui, J. Liu, J. Li, T. Zhang, *Nat. Chem.* **2011**, *3*, 634-641.

[13]   J. S. Luo, L. Steier, M. K. Son, M. Schreier, M. T. Mayer, M. Gratzel, *Nano Lett.* **2016**, *16*, 1848-1857.

[14]   T. Ohno, N. Murakami, T. Tsubota, H. Nishimura, *Appl. Catal. A*, *349*, 70-75.

[15]   J. Timoshenko, H. S. Jeon, I. Sinev, F. T. Haase, A. Herzog, B. Roldan Cuenya, *Chem. Sci.* **2020**, *11*, 3727-3736.

[16]   J. Timoshenko, A. Halder, B. Yang, S. Seifert, M. J. Pellin, S. Vajda, A. I. Frenkel, *J. Phys. Chem. C* **2018**, *122*, 21686-21693.

[17]   H. M. Liu, N. Guijarro, J. S. Luo, *J. Energy Chem.* **2021**, *61*, 149-154.

[18]   J. Wang, L. Yu, L. Hu, G. Chen, H. Xin, X. Feng, *Nat. Commun.* **2018**, *9*, 1795.

[19]   T. M. Masahiro Kohno, Toshihiko Ozawa and Yoshimi Niwano, *J. Clin. Biochem. Nutr.* **2011** *49*, 96-101.

[20]   L. L. Zhu, H. P. Lin, Y. Y. Li, F. Liao, Y. Lifshitz, M. Q. Sheng, S. T. Lee, M. W. Shao, *Nat. Commun.* **2016**, *7*, 12272.

Entry for the Table of Contents
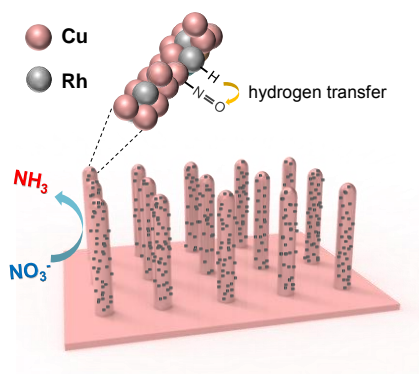
A novel copper nanowire supported rhodium cluster and single atom electrocatalyst (Rh@Cu) for NITRR was designed. Benefiting from the catalytic cooperation between Rh and Cu, whereby Rh activates the hydrogenation of *NO intermediate on Cu, Rh@Cu systems achieve a faradaic efficiency up to 93% at −0.2 V vs. RHE and a record ammonia yield rate of 1.27 mmol h^{-1} cm^{-2}.